

MIT Open Access Articles

Suspended Nanochannel Resonator Arrays with Piezoresistive Sensors for High-Throughput Weighing of Nanoparticles in Solution

The MIT Faculty has made this article openly available. **Please share** how this access benefits you. Your story matters.

Citation: Gagino, Marco et al. "Suspended Nanochannel Resonator Arrays with Piezoresistive Sensors for High-Throughput Weighing of Nanoparticles in Solution." ACS Sensors 5, 4 (April 2020): 1230–1238. © 2020 American Chemical Society

As Published: <http://dx.doi.org/10.1021/acssensors.0c00394>

Publisher: American Chemical Society (ACS)

Persistent URL: <https://hdl.handle.net/1721.1/132612>

Version: Author's final manuscript: final author's manuscript post peer review, without publisher's formatting or copy editing

Terms of use: Creative Commons Attribution-Noncommercial-Share Alike



Suspended Nanochannel Resonator Arrays with piezoresistive sensors for high-throughput weighing of nanoparticles in solution

Marco Gagino†‡#□Δ, Georgios Katsikis†Δ, Selim Olcum†⊥‡, Leopold Virots‡‡, Martine Cochet‡, Aurélie Thuaires‡, Scott R. Manalis†§||, Vincent Agache†‡**

* Corresponding authors

Δ Those co-authors contributed equally

* Those co-authors contributed equally

AUTHOR ADDRESS

† Koch Institute for Integrative Cancer Research, Massachusetts Institute of Technology, Cambridge, MA, USA

‡ Université Grenoble Alpes, CEA, LETI, 38000 Grenoble, France

Politecnico di Torino, Torino, Italy

□ Institut polytechnique de Grenoble, France

§ Department of Biological Engineering, Massachusetts Institute of Technology, Cambridge, MA, USA

|| Department of Mechanical Engineering, Massachusetts Institute of Technology, Cambridge, MA, USA

⊥ Travera, 700 North, Main St, Cambridge MA 02139

KEYWORDS.

Piezoresistive readout, NEMS, nanofluidic, nanoparticles, mass sensor.

ABSTRACT

As the use of nanoparticles is expanding in many industrial sectors, pharmaceuticals, cosmetics among others, flow-through characterization techniques are often required for in-line metrology. Among the parameters of interest, the concentration and mass of nanoparticles can be informative for yield, aggregates formation or even compliance with regulation. The Suspended Nanochannel Resonator (SNR) can offer mass resolution down to the attogram scale precision in a flow-through format. However, since the readout has been based on the optical lever, operating more than a single resonator at a time has been challenging. Here we present a new architecture of SNR devices with piezoresistive sensors that allows simultaneous readout from multiple resonators. To enable this architecture, we push the limits of nanofabrication to create implanted piezoresistors of nanoscale thickness (~ 100 nm) and implement an algorithm for designing SNRs with dimensions optimized for maintaining attogram scale precision. Using 8-inch processing technology, we fabricate parallel array SNR devices which contain ten resonators. While maintaining a precision similar to that of the optical lever, we demonstrate a throughput of 40,000 particles per hour – an order of magnitude improvement over a single device with an analogous flow rate. Finally, we show the capability of the SNR array device for measuring polydisperse solutions of gold particles ranging from 20 to 80 nm in diameter. We envision that SNR array devices will open up new possibilities for nanoscale metrology by measuring not only synthetic but also biological nanoparticles such as exosomes and viruses.

One of the current challenges for nanometrology¹ is the advancement of tools for quantifying physical properties of particles in solution with high precision as well as high throughput. This is necessary for studying naturally occurring nanoparticles and engineered nanoparticles (e.g., exosomes², viruses^{3,4}, protein aggregates, and assembled nanostructures as drug-delivery vehicles⁵) as well as for the quality control of synthetic nanoparticle products⁶. Several approaches are currently available⁷. Light scattering methods (including Dynamic Light Scattering DLS⁸, Static light scattering SLS⁹) measure the scattered-light fluctuations caused by the Brownian motion of particles in solution. These are ensemble-based methods that can be prone to errors related to variations in size, concentrations and optical properties of a given sample⁸. Resistive pulse sensing (RPS)^{10,11} is based on voltage variation while a nanoparticle passes through a nanofluidic constriction and enables single particle resolution but requires conductive electrolyte solutions. Nanoparticle Tracking Analysis (NTA)¹² also enables single particle resolution but requires nanoparticles that are either fluorescent or highly scattering.

The Suspended Nanochannel Resonator (SNR)¹³ is a category of nanomechanical mass sensors^{14,15,16,17} which measures nanoparticles in a flow-through manner to characterize their buoyant mass and concentration. It is based on a hollow cantilever beam with an embedded nanofluidic channel. The cantilever is externally driven to oscillate at its resonant frequency. The cantilever is packaged within a vacuum-sealed cavity to minimize dissipation with the surrounding medium and thereby maximize the quality factor Q ¹⁸. As a particle flows through the nanofluidic channel inside the cantilever, the resonant frequency is transiently modulated due to the buoyant mass of the particle. By pushing the limits of miniaturization¹⁹ and achieving a high quality factor ($Q > 1,000$), the SNR has achieved single attogram (10^{-18} g) precision¹³ which has enabled measurements from extracellular vesicles in the 20-200 nm range and gold nanoparticles down to

10 nm in diameter. Since this method relies on Archimedes principle, the mass, volume and density of a particle can be obtained by weighing it in solutions of different densities^{20,21}. Despite these capabilities, measurement throughput has been limited since only a single SNR has been used to date^{13,19}.

In contrast to SNRs, there are numerous examples where the throughput of cantilever sensors has been improved by using arrays with deflection readout based on various electrical^{22,23,24,25,26,27,28} and optical approaches²⁹. In our work, we have used piezoresistive sensors to enable both serial³⁰ and parallel³¹ arrays of Suspended Microchannel Resonators (SMRs) for particle characterization. Piezoresistive sensors^{32,33} were initially developed for microcantilevers as an alternative to optical level readout³⁴ as well as for measuring smaller cantilevers such as nanomechanical oscillators³⁵ where the optical requirements become more complex. Over the years, significant effort has been directed towards developing and optimizing piezoresistors based on metallic^{36,37} and semiconductor^{27,38,39,40} materials. Here we present a new architecture of SNR array devices with silicon piezoresistive sensors that allows simultaneous readout from multiple resonators. To enable this architecture, we push the limits of nanofabrication to create implanted piezoresistors of nanoscale thickness (~100 nm) and implement an algorithm for designing SNRs with dimensions optimized for maintaining attogram scale precision. Using 8-inch processing technology, we fabricate parallel array SNR devices which contain ten resonators. While maintaining a precision similar to that of the optical lever, we demonstrate a throughput of 40,000 particles per hour – an order of magnitude improvement over a single-cantilever device with an analogous flow rate.

Optimization and Parameter Sweep

As a starting point, we built upon *Piezo D*, an open source software for modeling the performance and guiding the design of piezoresistive cantilever beam sensors⁴¹. Although originally developed for the design of solid cantilever beams to measure force, the code is modular and can be applied and adapted to a variety of problems. Here, we modified the algorithm to incorporate the geometrical features of the hollow cantilever (**Figure 1b**) and also to convert frequency noise to mass-equivalent noise for a given measurement bandwidth (**Supporting Information 6**). Overall, we optimized for seven geometric parameters for the cantilever (**Figure 1b**), including its total length L and width W , and the height t_c and width w_c of the inner channel extending to the tip of the cantilever ($L_c = L - w_{ext}$); other parameters such as the thickness t_{LID} of the bottom and top lids sealing the embedded channel were assumed fixed, consistent with technological constraints (*i.e.* device layer thickness of SOI wafers). Simultaneously, we optimized for three geometric parameters for the piezoresistive elements including their length L_{PZR} , width W_{PZR} and thickness t_{PZR} .

While designing the optimization workflow (**Figure 1c**), we took simple process considerations into account (e.g. lithography resolution and overlay, minimum bonding area, selectivity of etching regarding the materials) in order to define the embedded channel dimensions and cantilever thickness and width. For example, we set the minimum channel dimensions to 700 nm to reduce clogging, and together with technological constraints, we set the minimum thickness t of the cantilever to 1.1 μm (equivalent to $t_{LID} = 200$ nm for both top and bottom lid, and 700 nm of channel depth t_c). We set the minimum width of the internal and external walls (w_{int} , and w_{ext}) to a conservative value of 500 nm to accommodate lithography alignment errors and to ensure

sufficient bonding area. We also assumed that the inner channel is placed precisely on the neutral axis of the beam to reduce the dissipation arising from pumping of the fluid⁴².

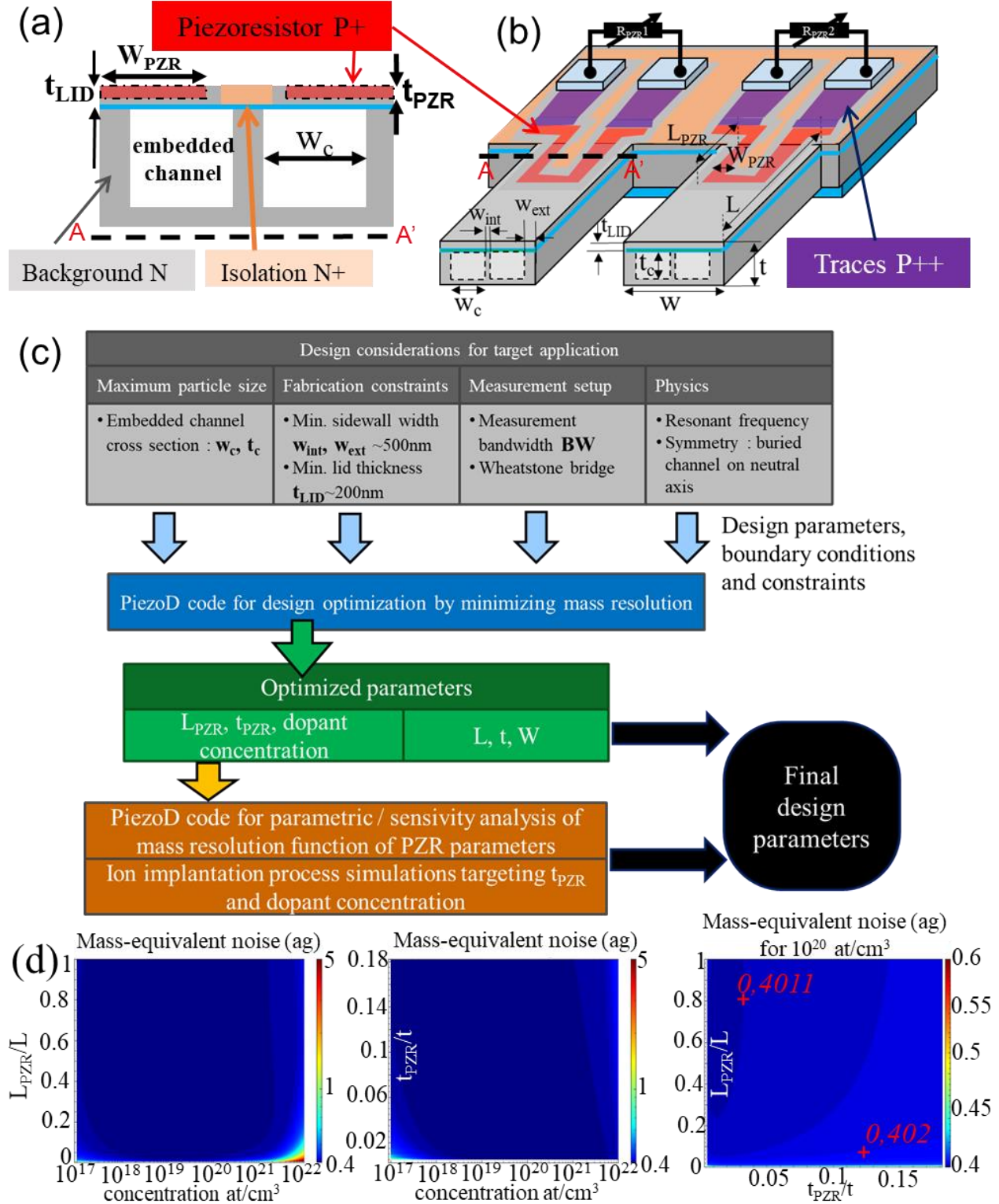


Figure 1: (a) and (b) Cross section and perspective view of the SNR showing the parameters defining the geometry of the device and the doping. L and W refer respectively to the cantilever length and width. The SNR features a U-shaped embedded fluidic channel of length L_c , width w_c , and depth t_c , extending to the free apex, with a separating internal wall of width w_{int} as well as external bounds of width w_{ext} to ensure hermeticity. We assume the thickness t_{LID} to be identical for both the bottom and top lids sealing the embedded channel. (c) Flow chart of optimization design algorithm for SNR. (d) Mass-equivalent noise analysis for a fixed design geometry (Array A1 SNR #10) function of the piezoresistor (PZR) parameters. The PZR doping profile is assumed constant over the PZR thickness. Left plot shows the evolution of the mass sensitivity as a function of the PZR length ratio and doping concentration when the PZR thickness (t_{PZR}/t) ratio is set to 0.1. Center plot is for constant PZR length ratio (L_{PZR}/L) of 0.4 whereas the right plot is for a constant doping concentration of 1×10^{20} at/cm³.

The goal of the optimization design is to achieve attogram mass-equivalent noise while accommodating a wide range of particle sizes in the SNR. To do so, we accounted for three noise sources (thermomechanical, 1/f Hooge noise, and the Johnson noise for the piezoreadout⁴¹) and assumed that the SNR is driven at the onset of non-linearity¹³. We thus optimized the SNR design for a given resonant frequency assuming a quality factor $Q = 1,000$ and a measurement bandwidth of 200 Hz. In the initial round of optimization, we considered a constant doping profile for the piezoresistor. As an example, targeting a resonant frequency of 0.5 MHz leads to a 2.8 ag mass-equivalent noise, whereas for 1.5 MHz and above, the mass-equivalent noise decreases below 1 ag (Table S2). In this example, the resulting doping concentration, length ratio (L_{PZR}/L) and thickness t_{PZR} for the piezoresistor are approximately 4.2×10^{19} at/cm³, ~33% and 100 nm (half the top lid thickness t_{LID}), respectively. For all cases, we found that the optimized mass-equivalent noise was close or equal to the thermomechanical limit, showing that the optimized piezoresistor design should not degrade the resolution.

To study the variation of mass resolution around the optimum design point, we performed a parametric study as a function of the piezoresistor length ratio (L_{PZR}/L), thickness ratio (t_{PZR}/t) and doping concentration (Figure 1d). We fixed the SNR geometry to the highest frequency of 2.5 MHz. As expected from the optimization, the mass-equivalent noise is optimized for a doping

concentration close to 10^{20} at/cm³, but has little sensitivity to the piezoresistor length ratio and thickness ratios in the doping concentration range 10^{19} - 10^{20} at/cm³. As long as $L_{PZR}/L > 0.05$, any change in the mass resolution relative to the thermomechanical limit is less than 1%.

For the second round of optimization, we studied the effect of the ion implantation doping profile of the piezoresistor on mass-equivalent noise by using Silvaco⁴³ software. We performed simulations for dopant concentrations in the range of 10^{19} to 10^{20} at/cm³ and a junction depth of ~100 nm relative to the surface of the top lip. We found that concentrations in this range resulted in a similar mass-equivalent noise (**Figure S1**). To ensure a well-controlled and robust ion implantation process, we chose 5 keV energy with implantation dose of 7×10^{14} at/cm². Although the length of each cantilever varies across our arrays, we used constant lengths of 14 and 10 μ m for all the piezoresistors of the cantilevers within the A0 and A1 arrays, respectively (see **Table 2**). This allowed for a simpler readout circuit configuration with amplification stages that were optimized for all devices. We found that the mass resolution varies about ~16% across the arrays (**Figure S2**).

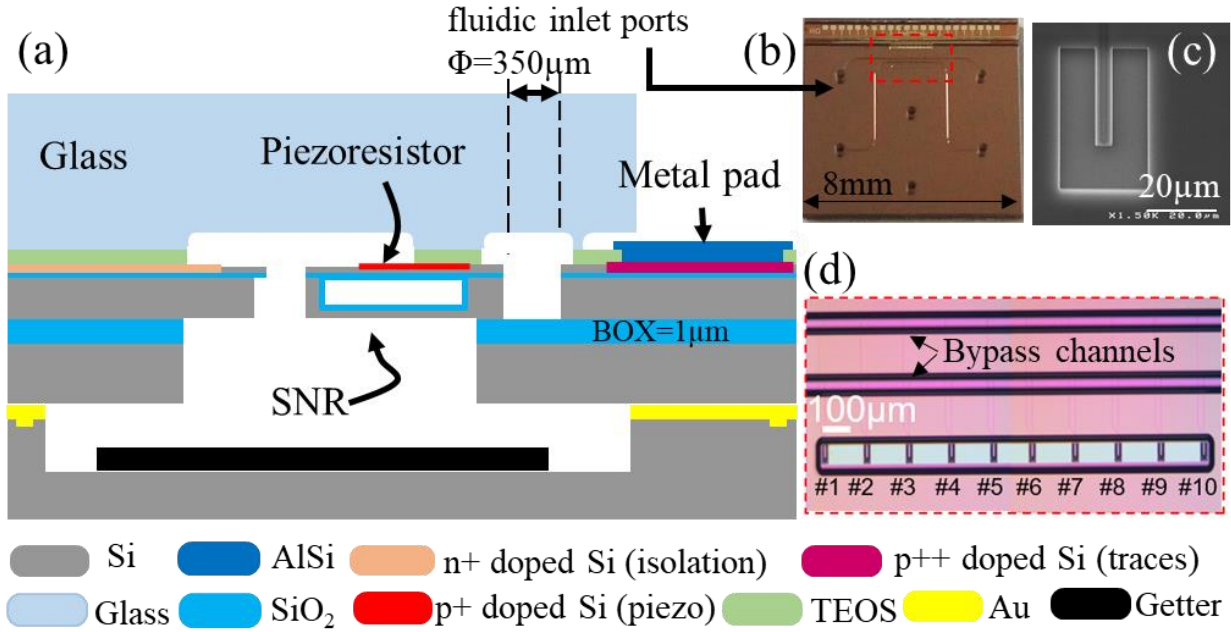


Figure 2: (a) Cross-section of a SNR illustrating the different materials implemented for operating the chip. The SNR structure is obtained from 2 SOI (Silicon On Insulator) wafers being bonded together (fusion bonding). The chip was hermetically sealed to a borofloat glass wafer through a TEOS (Tetra-Ethyl-Ortho-Silicate) interface layer. The glass wafer contains 4 inlet ports (350 μm in diameter) drilled through the entire substrate thickness for injection of the fluids, as well as 10 μm deep channels, and a dome above the SNRs to allow for their flexural out-of-plane oscillation. A bottom wafer with a getter was bonded underneath (by eutectic fusion under vacuum) for long-term vacuum sustainability. The piezoresistor in each SNR was built up from local p+ implantation of the top SOI layer. p++ type traces are connecting each piezoresistor to corresponding addressing metal pads. n++ isolation traces were also achieved by local implantation to create uniform p-n junction isolation of the piezoresistor from the substrate and limit the crosstalk with adjacent SNRs. (b) Bright field microscopy image of a SNR array die with ten SNRs embedded in the same vacuum-sealed cavity. The metal pads for addressing each SNR are placed away from the array, and the glass wafer is partially saw-diced and removed to expose the pads for wire bonding. (c) Scanning electron microscope image of a SNR0 cantilever. (d) Close-view bright field microscopy image of the marked region (dashed red rectangle) of SNR array shown in (b).

Fabrication of devices

Based on our optimization results, we fabricated two different types of SNR array devices A0 and A1 (**Figure 2a, b, Table 2**), with similar geometrical characteristics to those of single-resonator SNRs of type SNR0 and SNR1 respectively (**Figure 2c, Table 1**). To create distinct and evenly spaced resonance frequencies in the arrays, we used increments of 250 and 200 nm between successive cantilevers in the A0 and A1 arrays respectively. The piezoresistor of each SNR resonator within an array was individually connected electrically to a metallic pad. This enabled us to independently track the signal from each piezoresistor and thus realize a simultaneous readout of the resonance frequency for each SNR (**Figure S20**). The embedded fluidic channels were connected in parallel configuration across two opposite bypass channels (**Figure 2d**) etched in the glass wafer. Each cantilever incorporated a p-type piezoresistor which was locally implanted, forming a U-loop at the clamped end of the cantilever (**Figure 1b**) but mostly parallel to the $\langle 110 \rangle$ direction to maximize the gauge factor for the dopants. A getter was located in a cavity placed underneath the array for sustaining long-term vacuum sealing (**Figure 2a**).

$$t_c = 700 \text{ nm}$$

$$w_{ext} = 1 \text{ } \mu\text{m}$$

$$w_{int} = 500 \text{ nm}$$

Resonator type	f_0 (MHz)	L (μm)	R_m (mHz/ag)	W_c (nm)	W (μm)
SNR0	1.5	32.5	5	1000	4.5
SNR1	2.5	25	15	700	3.9

Table 1 : Summary of single-resonator SNR geometrical properties. t_c and w_c are the embedded channel depth and width, w_{int} and w_{ext} are the channel-to-channel and channel-to-sidewalls spacings, f_0 is the resonance frequency while the embedded channel is empty, L and w are the resonator's length and width, R_m is a typical value of mass sensitivity.

$$t_c = 700 \text{ nm}$$

$$W_c = 1 \text{ } \mu\text{m}$$

$$w_{int} = 500 \text{ nm}$$

A0 Resonator #	1	2	3	4	5	6	7	8	9	10
L (μm)	33.75	33.5	33.25	33	32.75	32.5	32.25	32	31.75	31.5
w_{ext} (μm)	1									
W (μm)	4.5									
f_0 (MHz)	1.40	1.42	1.44	1.46	1.48	1.50	1.53	1.55	1.58	1.60
R_m (mHz/ag)	4.46	4.57	4.67	4.78	4.89	5.00	5.12	5.24	5.36	5.50
A1 Resonator #	1	2	3	4	5	6	7	8	9	10
L (μm)	26.8	26.6	26.4	26.2	26	25.8	25.6	25.4	25.2	25
w_{ext} (μm)	0.5									
W (μm)	3.5									
f_0 (MHz)	2.23	2.27	2.30	2.34	2.37	2.41	2.45	2.49	2.53	2.57
R_m (mHz/ag)	15.2	15.5	15.8	16.2	16.6	16.9	17.3	17.7	18.2	18.6

Table 2 : Summary of parallel SNR arrays A0 and A1 geometrical properties.

Methods and setup

The deflection signal from each SNR in the array was amplified through a dedicated transimpedance amplifier-based circuitry. Then all the signals were summed through differential amplifiers to minimize common-mode noise and external interference in the system. After going through analog to digital circuitry, the sum signal was fed into a field-programmable gate array (FPGA) board (Cyclone IV FPGA, Altera). The FPGA board is designed to sustain an array of 14-bit phase-locked loop (PLL) controllers, for which implementation details had been published previously⁴⁴. Briefly, each PLL in the FPGA was locked to the unique resonant frequency of a single SNR cantilever in the array (**Figure S16**). The parameters of the PLL controller were determined based on the resonant frequency and quality factor of the corresponding SNR as well as the desired closed loop response (bandwidth, order) of the PLL controller-resonator system (**Figure S18**)⁴⁴. The instantaneous frequency of the numerically controlled oscillator of each PLL was used to create a sinusoidal signal and then all the frequency signals were summed together to create a drive signal to vibrate a single piezoceramic plate that simultaneously actuated the entire SNR array. We experimentally found the n-type background substrate bias should be set to 1 V to ensure an optimized n-p isolation across the different cantilevers within the array and limit the noise. The measured resonance frequency was post processed with a MATLAB script which extracted frequency peak shifts arising from a particle passage event using matched filters of varying peak widths¹³ mimicking a particle passing through the embedded channel. Four independently pressurized vials were fluidically connected to the two bypass channels for the SNR array: one channel was used for loading the nanoparticles and the other for collecting them after their measurement. All channels were rinsed with filtered de-ionized water for ~10 minutes after each measurement was completed to ensure that no residual nanoparticles from previous

measurement remained in the cantilevers. Different dilutions of calibrated gold nanoparticles (BBI solutions) were prepared by mixing the original samples with filtered buffer solution.

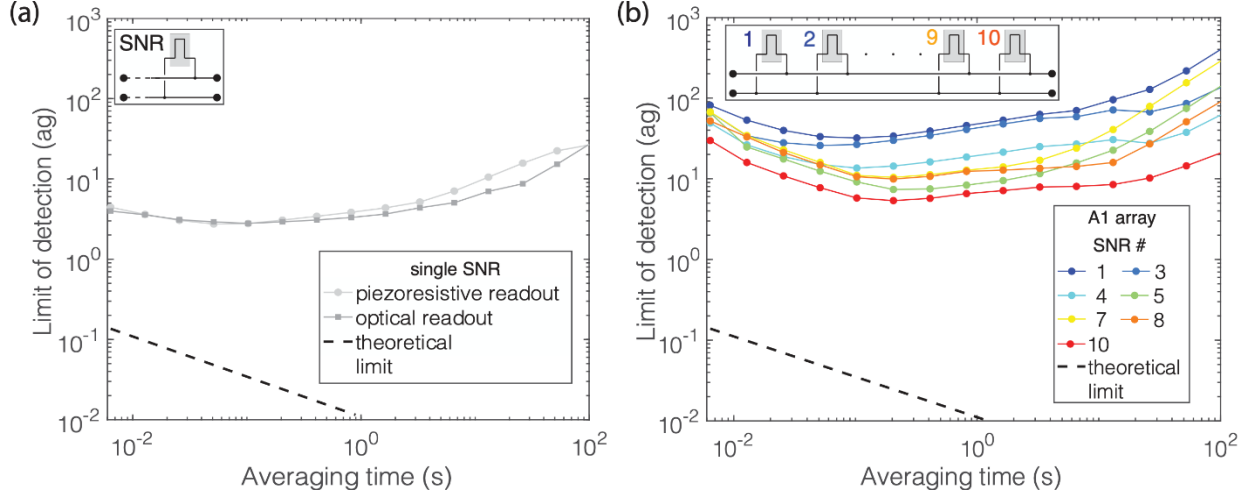


Figure 3: Frequency stability analysis of SNRs. (a) Limit of detection of buoyant mass vs averaging time for a single-resonator SNR (#10 from array A1, quality factor $Q=1,979$) based on the noise baseline of resonance frequency using piezoresistive (light grey circles) and optical (dark grey squares) readout for measurement bandwidth of 1,000 Hz. The Allan deviation was extracted and converted into the corresponding limit of detection for buoyant mass. The black dashed line shows the theoretical minimum limit (**Supplementary Information 6**). Inset shows top view schematic of cantilever (grey box) where black lines denote the fluidic channels and black dots the fluidic inlets and outlets. (b) Limit of detection of buoyant mass versus averaging time for a parallel SNR A1 array (each curve of colored circles corresponds to same color numbers indexing each cantilever in the inset schematic) with seven resonators ($Q=1,800-2,100$) simultaneously locked through their PLL loop⁴⁴. The rest of experimental settings and symbols are same as in (a). All measurements of (a) and (b) are performed without liquid in the resonators.

Piezoresistive readout exhibits similar mass-equivalent noise as the optical readout

We first tested our SNR devices without particles flowing through in order to evaluate their noise performance or equivalently their mass resolution. In particular, we calculated the mass-equivalent noise by measuring the resonance frequency fluctuations, extracting the Allan deviation and converting it into mass (**Supporting Information 6**). We used this mass-equivalent noise to compare the performance of the piezoresistive readout to the optical readout method described in previous work¹³. We acquired data for 15 minutes with a sampling rate of 10 kHz for cantilevers not containing liquid. We found that the piezoresistive readout from a single cantilever ($Q=1,979$) exhibited a mass-equivalent noise of 3 ag with a 1 kHz bandwidth, similar to what we observed

with the optical readout (**Figure 3a**). For the SNR array device, we found that the cantilevers ($Q=1,800-2,100$) when operated simultaneously exhibited a slightly larger mass-equivalent noise of 6-40 ag with a 1 kHz bandwidth (**Figure 3b**). However, unlike the single cantilevers (**Figure S17**), cross-talk between cantilevers within the array prevented us from simultaneously driving them towards the non-linearity regime.

Performance metrics of the SNR array device

By testing over a hundred SNR array devices, we found that there were typically 7 – 9 operational cantilevers out of the array of 10 (**Figure S19a**) and the total resistance of the readout path for these cantilevers was measured in the range 5-6 k Ω as opposed to non-functional cantilevers that had resistances over 1 M Ω . Quality factor values of cantilevers within the array ranged from 100 to 5,000 (**Figure S19b**). To enable optimal closed-loop operation and minimize the risks of crosstalk with adjacent cantilevers, we experimentally found it was necessary for the quality factor Q to be above 500.

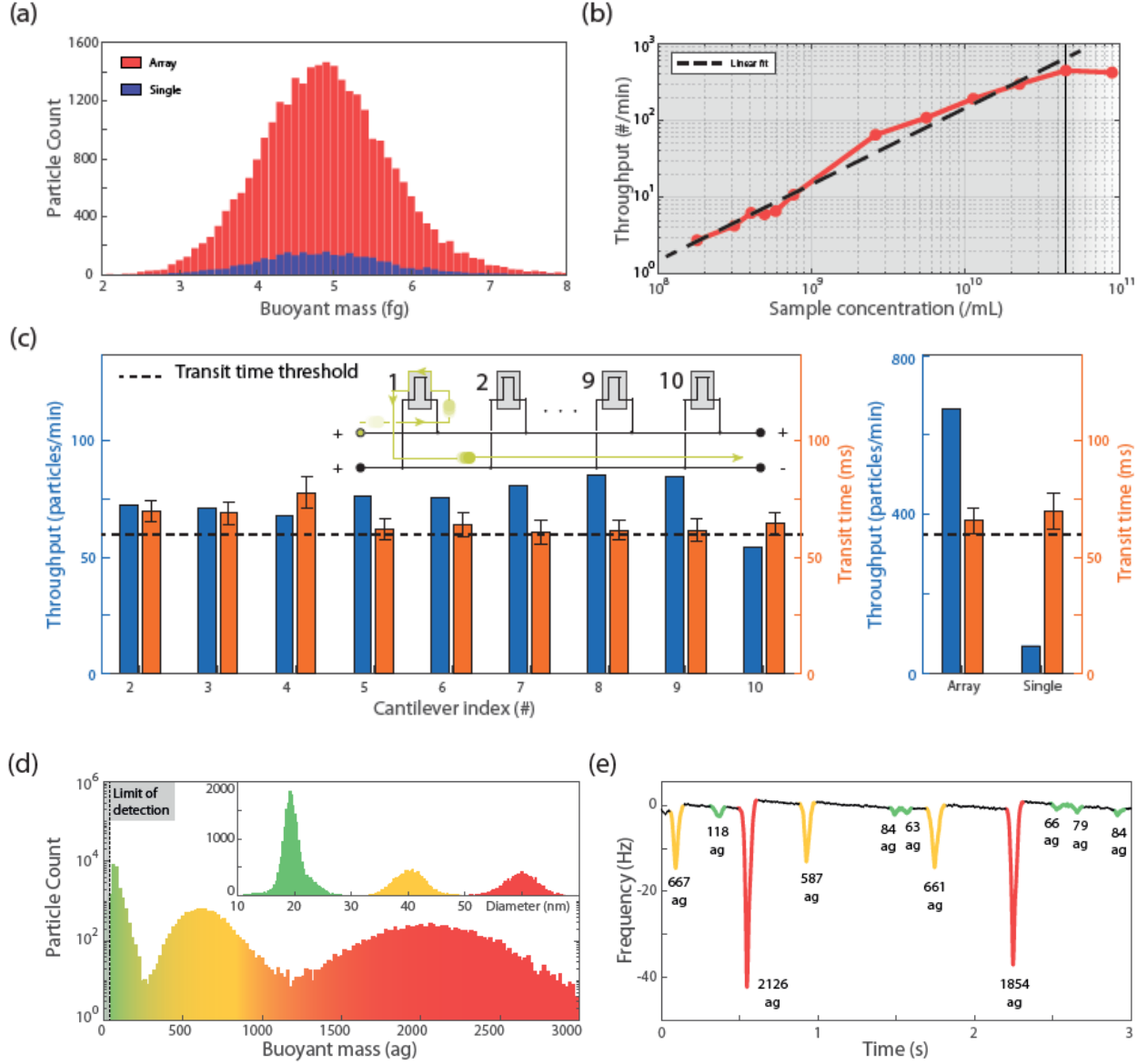


Figure 4: Performance of parallel SNR arrays. (a) Buoyant mass distribution of 80 nm-diameter gold nanoparticles measured with a parallel SNR array of 9 resonators having quality factors between 180 and 840, and a single-resonator SNR (Table 1, Table 2). The measurement bandwidth was 200 Hz and the flow rate was set so that the transit time was above $\geq 12 / 200$ Hz, based on our analysis on transit time limit (Figure S22). (b) Average throughput of 4 resonators in a parallel SNR array measuring suspensions of 40 nm-diameter gold nanoparticles with concentrations ranging from 0.18×10^9 to 90×10^9 nanoparticles/mL. For all tested sample concentrations, we used the same measurement time of 5 minutes. (c) Comparison of throughput and particle transit times for the experiment in a) between a parallel SNR array with 9 resonators and single-resonator SNR. The transit time of each nanoparticle was computed using an existing MATLAB algorithm¹³ that extracts the time difference between when the nanoparticle entered and exited the resonator. The inset in (c) shows a schematic of the parallel SNR array used for measuring the particles. The flow in the top bypass channel was pinched (high pressure at both inlets) to force the sample to flow from the left inlet into the embedded channel of the resonators.

(d, e) Polydisperse sample measurement through a parallel SNR array with 4 resonators. A mixture was prepared containing 20 nm, 40 nm and 60 nm-diameter gold nanoparticles (represented with green, yellow, red colors, respectively) in resulting concentrations of 7×10^9 , 4×10^9 , and 3×10^9 particles/mL, respectively (d) Buoyant mass measurement and diameter estimate (inset) of the three population subsets of nanoparticles. (e) Resonance frequency shift peaks versus time corresponding to the passage of gold nanoparticles through the resonators. Numbers indicate buoyant mass in ag and colors correspond to coloring scheme in (d).

Next, we compared the throughput of the SNR array to a single SNR device. As expected, the throughput increase is proportional to the number of operational cantilevers within the array for a given particle concentration and flow rate (**Figure 4a**). We demonstrated this enhancement with a sample of calibrated 80 nm-diameter gold nanoparticles (BBI Solutions), diluted in filtered de-ionized water with a concentration of 3.3×10^9 nanoparticles/mL and a transit time through the cantilever of 69.8 ms in the single SNR and 65.5 ms in the SNR array (average value across the set of operational cantilevers). We achieved the maximum throughput using an SNR array with nine operational cantilevers which measured approximately 670 nanoparticles/minute (total of 29,347 particles measured over 44 minutes) compared to a single SNR device which measured approximately 70 nanoparticles/minute (total of 3,133 particles measured over 44 minutes). For the SNR array device and the single SNR device, the estimated coefficients of variation in diameter were $CV=5.7\%$, and 5.6% , respectively, in agreement with the $CV<8\%$ reported by the manufacturer (**Figure S21**). After adjusting the flow pressures so that all transit times in the array device were above the threshold for accurately capturing the shape of the peak, we found that the transit time varied up to 25% across the cantilevers (**Figure 4c**).

To quantify the range of sample concentration that can be measured with the SNR array, we measured the throughput for 40 nm-diameter gold nanoparticles at concentrations ranging from 10^8 to 10^{11} particles/mL (**Figure 4b**). At higher concentrations, measurement of single particles became less frequent due to the increased likelihood of more than one particle being present inside

the cantilever at the same time (**Figure S23**). At lower concentrations, the number of particle counts per time decreased and we found that longer measurement time windows were needed to create a robust histogram. Overall, we found that the throughput of nanoparticles measured by the SNR array scales linearly with sample concentration up to a maximum limit of approximately 4×10^{10} nanoparticles/mL (**Figure 4b**), where coincidence of nanoparticles transit events begins to occur.

Moreover, we demonstrated the ability of the SNR array to characterize polydisperse samples by measuring a mixture of 20 nm, 40 nm, and 60 nm-diameter gold nanoparticles (**Figure 4d,e**) using an SNR array with a mass-equivalent noise of 20-40 ag (**Figure S24**). To clearly distinguish the baseline noise from the frequency response from transiting particles (**Figure 4e**, green peaks), we set the limit of detection threshold to 47 ag (the buoyant mass of 20 nm-diameter gold nanoparticles is 77 ag) and the measurement bandwidth to 150 Hz to accommodate nominal transit times of 100 ms. This resulted in a throughput of 440 nanoparticles/minute. We observed that the average transit time and its standard deviation was similar for all three subsets of nanoparticles (**Figure S25**).

Conclusion

Given the mass-equivalent noise of 6-40 ag in our SNR array devices (**Figure 3b**), we envision measuring nanoparticles less dense than gold, such as exosomes¹³ (40 to 150 nm diameter exosomes have a buoyant mass ranging from 10 to 200 ag) and medium-sized viruses⁴⁵ (a bacteriophage T7 of approximate diameter 50 nm has a buoyant mass of 30 ag; a HIV virion of approximate diameter 120 nm has a buoyant mass of 80 ag). There is a large margin for further improving signal-to-noise in next generation devices. For the devices presented here, we conservatively designed the thickness of cantilever walls to be of the order 0.5 μm (w_{int} , w_{ext} on **Figure 1**) to ensure fabrication robustness. However, we also designed and fabricated devices with

thicknesses of 0.25 μm (**Figure S26**) which were not used in this work because the microfluidic packaging for weighing nanoparticles was not readily available. In fact, we validated the fabrication robustness by filling the cantilevers with liquid using capillary forces and measuring the frequency shift compared to cantilevers without liquid. In subsequent generations, we can reduce wall thickness by a factor of two (i.e. to 0.25 μm) or more and widen the cross-section area of the embedded channel to increase the nanoparticle size range without increasing the effective mass of the resonators or compromising integrity. For example, increasing the embedded channel dimensions to 2x2 μm^2 (from 0.7x1 μm^2 used in the present work) would only increase the equivalent mass noise by 30% compared to the current design (**Table S3**). Moreover, we observed that the yield of our devices with high quality factor ($Q>1,000$) was less than 30%, which was due to the failure of the sealing of the vacuum chamber. To increase yield, we can increase the contact area for the interface layer sealing the vacuum chamber (TEOS layer on the **Figure 2**).

The measurement throughput can be further increased by scaling up the number of cantilevers per SNR device, which is theoretically possible yet it requires practical considerations. For example, an increase from ten to fifty resonators would entail straightforward adaptations such as increasing the surface area of the device and using a field-programmable-gate-array with higher read-out capacity. The measurement throughput per cantilever can also be increased by flowing the particles faster than the transit time threshold (**Figure S22**) and applying a convolution algorithm³¹ to correct the distorted measured frequency peak and recover the actual particle mass. However, scaling up the number of resonators in parallel array SNRs entails several limitations that must be considered. First, each cantilever in a parallel SNR needs to operate at a discrete resonance frequency to avoid crosstalk with other cantilevers. To attain a discrete resonance frequency, each cantilever is designed with a discrete length, resulting in different effective masses

and sensitivities. Thus, increasing the number of cantilevers in an array would result in a variation in mass equivalent noise among cantilevers. For example, for an array of fifty cantilevers with the shortest cantilever having a length of 25 μm and an increment of 200 nm in length for the rest, the lowest frequency cantilever (35 μm long) would have two times the mass equivalent noise of the highest frequency cantilever (25 μm long) (**Figure S2**). Second, the pressure difference between the inlet and outlet of each cantilever may vary because it depends on its position within the array, and the total length of both the embedded channel in the cantilever and the channels connecting it to each bypass channel (**Figure 2d**). This potentially results in non-uniform transit times across the array. To ensure that the transit time through all the cantilevers is nearly uniform as it is in the case of an array of ten SNRs (**Figure S25**) additional considerations should be made in the design and the fluidic setup.

Finally, we envision SNR devices, connected to upstream microfluidic sample preparation modules, such as acoustofluidics⁴⁶, or Deterministic Lateral Displacement⁴⁷, for a workflow including size-sorting purification and mass measurement of isolated species. As both techniques separate particles by size, preserving their integrity, their outlet could be connected to SNRs arrays with cross-sections tailored to the size range of particles sorted upstream in order to provide analysis over the entire size range of a given sample.

Experimental section: SNR fabrication

The devices were fabricated from 8-inch (200 mm) MEMS wafer processing technology at CEA/LETI (**Supporting Information 3**). First, a SOI bottom wafer was patterned to delineate the embedded channel which is 700 nm deep. This wafer was then assembled with a top SOI wafer by direct fusion bonding. The top SOI handle substrate and BOX layer were removed successively

by coarse and then fine grinding followed by buffered HF etching to release the membrane covering the channel. Prior to release of the SNR cantilever from the SOI wafer, four ion implantation steps were added to create the piezoresistor (boron, p-type) in the top silicon layer of the wafer stack, including low-resistivity traces for connections between the piezoresistors and the metal pads, and n-type areas doped with phosphorous for electrical isolation. All the doping related process steps were supported by ion implantation and annealing simulations using Silvaco (see **Figure S11 to Figure S15 in Supporting Information 4**). Aluminum pads were patterned on highly-doped traces connecting the piezoresistor with the bond pads to further decrease the electrical resistance, except on areas for anodic bonding between the silicon wafer and the top glass wafer to ensure hermeticity. The SNR outer delineation was then defined by front-side lithography and RIE etching. The SNR resonator was released from the backside by photolithography and ICP RIE etching of both the bulk silicon underneath and the bottom SOI buried oxide (BOX) layer. The devices were connected in bypass configuration with lateral fluidic channels etched in a glass wafer anodically bonded onto the SOI layers for fluid exchange and sample injection. Inlet ports were drilled into the glass wafer for connection with external tubing. Finally, each cantilever was embedded in a vacuum sealed cavity enabled by a eutectic bonding with a bottom substrate hosting a getter material.

Fluids preparation

All fluids (including buffer fluid for rinsing) were prepared from de-ionized water filtered two times with 200 nm filters. Gold nanoparticles samples have been prepared from BBI Solutions (EM.GC20, EM.GC40, EM.GC60, EM.GC80, for Gold Nanoparticles of 20 nm, 40 nm, 60 nm, 80nm in diameter), and were suspended in the same solution than the buffer fluid.

ASSOCIATED CONTENT

Supporting Information.

The Supporting Information is available free of charge at: link to be provided by ACS.

The supporting information contains a nomenclature table for the acronyms used in the manuscript as well as details on the SNR design, optimization and fabrication. We present simulations results on dopants implantation and annealing steps that were used in the fabrication. We also provide details on the readout circuitry for implementing N PLL in parallel as well as the methodology for calculating the equivalent mass noise. Experimental results supporting the experiments section of the main manuscript are also included.

Corresponding Authors

*S.R. M. E-mail: srm@mit.edu

*V. A. E-mail : vincent.agache@cea.fr

Competing interests: Scott R Manalis: is a co-founder of Travera and Affinity Biosensors, which develops techniques relevant to the research presented. The other authors declare that no competing interests exist.

Author Contributions

V.A., M. G., S.O., G. K., S. R. M. contributed to the design of the study.

L. V., S.O., V.A., contributed to the design and modeling of the SNRs (geometry, piezoresistor optimization).

M.G., G. K., V. A. and S.O. performed the experiments and analyzed the data.

M.C., V.A., A.T., contributed to the fabrication of the SNRs.

V.A., M.G., G. K., L.V., S. R. M. contributed to the writing of the manuscript.

V.A., and S. R. M contributed to project management

Funding Sources

This research was supported by the LETI Carnot Institute EVEREST project, the outgoing CEA fellowships (V. A.) from the CEA-Enhanced Eurotalents program, cofunded by FP7 Marie Skłodowska-Curie COFUND program (Grant Agreement 600382), the Fulbright fellowship for the France National Researcher program (V.A.) and by the Institute for Collaborative Biotechnologies through grant W911NF-09-0001 from the US Army Research Office (S.R.M).

ACKNOWLEDGMENT

The authors thank Max Stockslager for support and fruitful discussions on the PLL limitations applied to an array of SMRs, Scott Knudsen on various aspects of the experimental setup, and François Baléras for the fabrication of SNRs.

REFERENCES

-
- ¹ Kim, H.-A.; Seo, J.-K.; Kim, T.; and Lee, B.-T. Nanometrology and its perspectives in environmental research, *Environ Health Toxicol.* **2014**; 29: e2014016, doi: [10.5620/eh.t.e2014016](https://doi.org/10.5620/eh.t.e2014016)
- ² Sheridan, C. Exosome cancer diagnostic reaches market, *Nature Biotechnology*, **2014**, 34, 359–360
- ³ Zamora, J. L. R.; Aguilar, H.C. Flow virometry as a tool to study viruses, *Methods*, **2018**, 134–135, 87–97
- ⁴ Ruz, J. J.; Tamayo, J.; Pini, V.; Kosaka, P.M.; Calleja, M. Physics of Nanomechanical Spectrometry of Viruses, *Scientific Reports*, **2014**, 4, 6051, doi: [10.1038/srep06051](https://doi.org/10.1038/srep06051)
- ⁵ Liu, Z.; Jiang, W.; Jiang, W.; Nam, J.; Moon, J.-J.; Kim, B. Y. S. Immunomodulating Nanomedicine for Cancer Therapy *Nano Lett.* **2018**, 18, 6655–6659
- ⁶ Bobo, D.; Robinson, K. J.; Islam, J.; Thurecht, K. J.; Corrie, S. R. Nanoparticle-Based Medicines: A Review of FDA-Approved Materials and Clinical Trials to Date, *Pharm Res* (**2016**) 33:2373–2387
- ⁷ Modena, M. M.; Rühle, B.; Burg, T. P.; and Wuttke, S. Nanoparticle Characterization: What to Measure?, *Adv. Mater.* **2019**, 1901556, doi: [10.1002/adma.201901556](https://doi.org/10.1002/adma.201901556)
- ⁸ Stetefeld, J.; McKenna, S. A.; Patel, T. R. Dynamic light scattering: a practical guide and applications in biomedical sciences. *Biophys. Rev.* **2016**, 8, pp. 409–427
- ⁹ Wyatt, P. J. Measurement of Special Nanoparticle Structures by Light Scattering. *Anal. Chem.* **2014**, 86, 7171–7183.
- ¹⁰ Fraikin J.-L., Teesalu T., McKenney C. M., Ruoslahti E., and Cleland A. N., A high-throughput label-free nanoparticle analyser, *Nature Nanotechnology* May **2011**, Vol. 6., pp. 308–313
- ¹¹ Vogel R, Willmott G., Kozak D., Roberts G. S., Anderson W., Groenewegen L., Glossop B., Barnett A., Turner A., and Trau M., Quantitative Sizing of Nano/Microparticles with a Tunable Elastomeric Pore Sensor, *Anal. Chem.* **2011**, 83, pp. 3499–3506
- ¹² Filipe, V.; Hawe A.; Jiskoot W., Critical evaluation of Nanoparticle Tracking Analysis (NTA) by NanoSight for the measurement of nanoparticles and protein aggregates, *Pharm Res.*, **2010** May; 27(5):, pp. 796–810.
- ¹³ Olcum, S.; Cermak, N.; Wasserman, S. C.; Christine, K. S.; Atsumi, H.; Payer, K. R.; Shen, W. J.; Lee, J. C.; Belcher, A. M.; Bhatia, S. N.; Manalis, S. R.; Weighing nanoparticles in solution at the attogram scale, *Proc. Natl. Acad. Sci. U. S. A.* **2014**, 111 (4), pp. 1310–1315.
- ¹⁴ Ekinci KL.; Yang, YT, Roukes ML, Ultimate limits to inertial mass sensing based upon nanoelectromechanical systems. *J Appl Phys*, **2004**, 95(5), pp. 2682–2689.
- ¹⁵ Yang Y. T., Callegari C., Feng X. L., Ekinci K. L., Roukes M. L., Zeptogram-Scale Nanomechanical Mass Sensing, *Nano Lett.* **2006**, 6, 4, pp. 583–586
- ¹⁶ Stassi, S. ; Marini, M. ; Allione, M., Lopatin, S. ; Marson, D. ; Laurini, E. ; Priel, S. ; Pirri, C. F. ; Ricciardi, C. ; Di Fabrizio, E. Nanomechanical DNA resonators for sensing and structural analysis of DNA-ligand complexes. *Nat Commun* **10**, 1690 (**2019**). <https://doi.org/10.1038/s41467-019-09612-0>
- ¹⁷ Yuksel, M.; Orhan, E.; Yanik C., Ari A. B., Demir A., Hanay M. S., Nonlinear Nanomechanical Mass Spectrometry at the Single-Nanoparticle Level, *Nano Lett.* **2019**, 19, 6, 3583–3589
- ¹⁸ Burg, T. P.; Godin, M.; Knudsen, S. M.; Shen, W.; Carlson, G.; Foster, J. S.; Babcock, K.; Manalis, S. R. *Nature* **2007**, 446 (7139), pp. 1066–1069.
- ¹⁹ Lee, J.; Shen, W.; Payer, K.; Burg, T. P.; and Manalis, S. R. Toward Attogram Mass Measurements in Solution with Suspended Nanochannel Resonators, *Nano Lett.*, **2010**, 10, 7, pp. 2537–2542
- ²⁰ Bryan A. K.; Hecht, V. C.; Shen, W.; Payer, K.; Grover, W. H.; Manalis, S. R. “Measuring Single Cell Mass, Volume, and Density with Dual Suspended Microchannel Resonators.” *Lab Chip* 14, no. 3 (**2014**), pp. 569–576
- ²¹ Grover, W.H.; Bryan, A.K.; Diez-Silva, M.; Suresh. S.; Higgins. J.M.; Manalis. S.R. Measuring single-cell density, *Proceedings of the National Academy of Sciences*, **2011**, 108 (27), pp. 10992–10996.

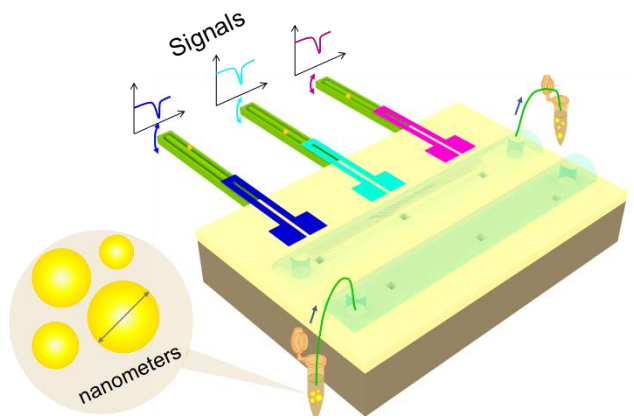
- ²² Ekinici KL, Roukes ML, Electromechanical transducers at the nanoscale: Actuation and sensing of motion in nanoelectromechanical systems (NEMS). **2005**, Small 1(8-9), pp. 786–797.
- ²³ Truitt, P. A.; Hertzberg, J. B.; Huang, C. C.; Ekinici, K. L.; Schwab, K. C. Efficient and Sensitive Capacitive Readout of Nanomechanical Resonator Arrays, Nano Lett. **2007**, 7, 1, pp. 120-126
- ²⁴ Ivaldi, P.; Abergel, J.; Matheny, M. H.; Villanueva, L. G.; Karabalin, R. B.; Roukes, M. L.; Andreucci, P.; Hentz, S.; Defaÿ, E. 50 nm thick AlN film-based piezoelectric cantilevers for gravimetric detection, J. Micromech. Microeng., **2011**, 21, 085023, DOI: 10.1088/0960-1317/21/8/085023
- ²⁵ Sage, E.; Sansa, M.; Fostner, S.; Defoort, M.; Gély, M.; Naik, A. K.; Morel, R.; Duraffourg, L.; Roukes, M. L.; Alava, T.; Jourdan, G.; Colinet, E.; Masselon, C.; Brenac, A.; and Hentz, S.; Single-particle mass spectrometry with arrays of frequency-addressed nanomechanical resonators, Nat Commun **9**, 3283, **2018**, <https://doi.org/10.1038/s41467-018-05783-4>
- ²⁶ Kouh, T.; Hanay, M. S.; Ekinici, K. L.; Nanomechanical Motion Transducers for Miniaturized Mechanical Systems, Micromachines **2017**, 8(4), 108., doi: [10.3390/mi8040108](https://doi.org/10.3390/mi8040108)
- ²⁷ Saya, D.; Belaubre, P.; Mathieu, F.; Lagrange, D.; Pourciel, J.-B.; Bergaud C. Si-piezoresistive microcantilevers for highly integrated parallel force detection applications, Sensors and Actuators A 123–124, **2005**, pp. 23–29
- ²⁸ Dominguez-Medina, S.; Fostner, S.; Defoort, M.; Sansa, M.; Stark, A.-K.; Halim, M. A.; Vernhes, E.; Gely, M.; Jourdan, G.; Alava, T.; Boulanger, P.; Masselon, C.; Hentz, S. Neutral mass spectrometry of virus capsids above 100 megadaltons with nanomechanical resonators, Science, **Nov. 2018**, 362 (6417), pp. 918–922
- ²⁹ Sampathkumar, A.; Ekinici, K. L.; Murray, T. W. Multiplexed Optical Operation of Distributed Nanoelectromechanical Systems Arrays. Nano Letter, **2011**, 11 (3), pp. 1014-1019.
- ³⁰ Cermak, N.; Olcum, S.; Delgado, F.F.; Wasserman, S.C.; Payer, K.R.; Murakami, M.; Knudsen, S.M.; Kimmerling, R.J.; Stevens, M.M.; Kikuchi, Y.; Sandikci, A.; Ogawa, M.; Agache, V.; Baléras, F.; Weinstock, D.M.; Manalis, S.R. High-throughput single-cell growth measurements via serial microfluidic mass sensor arrays, Nature Biotechnology, **2016**, 34, pp. 1052–1059.
- ³¹ Stockslager, M.A.; Olcum, S.; Knudsen, S.M.; Kimmerling, R.J.; Cermak, N.; Payer, K.; Agache, V.; Manalis, S.R.; Rapid and high-precision sizing of single particles using parallel suspended microchannel resonator arrays and deconvolution, Rev. Sci. Instrum. 90, **2019**, 085004; doi: 10.1063/1.5100861
- ³² Aikele, M.; Bauer, K.; Ficker, W.; Neubauer, F.; Prechtel, U.; Schalk, J.; Seidel, H. Resonant accelerometer with self-test. Sensors and Actuators A: Physical 92 (1-3), **2001**, pp. 161-167.
- ³³ Barlian, A.A.; Park, W.-T.; Mallon Jr, J. R.; Rastegar, A. J.; Pruitt, B. L. Review: Semiconductor Piezoresistance for Microsystems, Proc IEEE Inst Electr Electron Eng., **2009**; 97(3), pp. 513–552
- ³⁴ Tortonese, M.; Yamada, H.; Barret, R.C.; Quate, C.F. Atomic Force Microscopy Using a Piezoresistive Cantilever, Proceedings of IEEE Transducers **1991**, Pennington, pp. 448–451
- ³⁵ Li, M.; Tang, H. X.; Roukes, M. L., Ultra-sensitive NEMS-based cantilevers for sensing, scanned probe and very high-frequency applications, Nature Nanotechnology, **2007**, 2 (2), pp. 114–120
- ³⁶ Bargatin, I.; Myers, E.B.; Aldridge, J.S.; Marcoux, C.; Brianceau, P.; Duraffourg, L.; Colinet, E.; Hentz, S.; Andreucci, P.; Roukes, M.L. Large-scale integration of nanoelectromechanical systems for gas sensing applications. Nano Lett. **2012**, 12 (3), pp. 1269–1274.
- ³⁷ HDR dissertation of S. Hentz, “Downscaling silicon resonant MEMS and NEMS sensors: devices, transduction, non-linear dynamics and applications”, **2012**, <https://tel.archives-ouvertes.fr/tel-00740800/file/HDR.pdf>
- ³⁸ Hanay, M. S.; Kelber, S.; Naik, A. K.; Chi, D.; Hentz, S.; Bullard, E. C.; Colinet, E.; Duraffourg, L.; Roukes, M. L. Single-protein nanomechanical mass spectrometry in real time. Nat. Nanotechnol. **2012**, 7 (9), pp. 602–608.
- ³⁹ Mile, E.; Jourdan, G.; Bargatin, I.; Labarthe, S.; Marcoux, C.; Andreucci, P.; Hentz, S.; Kharrat, C.; Colinet, E.; Duraffourg, L. In-plane nanoelectromechanical resonators based on silicon nanowire piezoresistive detection. Nanotechnology, 21, **2010**, 165504, doi: 10.1088/0957-4484/21/16/165504
- ⁴⁰ Sage, E.; Brenac, A.; Alava, T.; Morel, R.; Dupré, C.; Hanay, M.S.; Roukes, M.L.; Duraffourg, L.; Masselon, C.; Hentz, S. Neutral particle mass spectrometry with nanomechanical systems, Nature Communications., 6, **2015**, 6482, DOI: 10.1038/ncomms7482
- ⁴¹ Doll, J. C.; Park, S.-J.; Pruitt, B. L. Design optimization of piezoresistive cantilevers for force sensing in air and water, Journal of Applied Physics **2009** Sep 15; 106(6): 064310, doi: [10.1063/1.3224965](https://doi.org/10.1063/1.3224965)
- ⁴² Sader, J.E.; Lee, J.; Manalis, S.R.; Energy dissipation in microfluidic beam resonators: Dependence on mode number, J Appl Phys. **2010** Dec 1;108(11):114507, DOI:[10.1063/1.3514100](https://doi.org/10.1063/1.3514100)
- ⁴³ Silvaco Deckbuild. www.silvaco.com. Internet, 2007
- ⁴⁴ Olcum, S.; Cermak, N.; Wasserman, S.C.; Manalis, S.R. High-speed multiple-mode mass-sensing resolves dynamic nanoscale mass distributions, Nature Communications, **2015**, 6, Article number: 7070, <https://doi.org/10.1038/ncomms8070>

⁴⁵ Gelderblom, H. R. Structure and Classification of Viruses, Medical Microbiology. 4th edition, **1996**.

⁴⁶ Wu, M.; Ouyang, Y.; Wang, Z.; Zhang, R.; Huang, P.H.; Chen, C.; Li, H.; Li, P.; Quinn, D.; Dao, M.; Suresh, S.; Sadosky, Y.; Huang, T.J. Isolation of exosomes from whole blood by integrating acoustics and microfluidics, Proceedings of the National Academy of Sciences, Oct **2017**, 114 (40), pp. 10584-10589

⁴⁷ Pariset, E.; Parent, C.; Fouillet, Y.; Boizot, F.; Verplanck, N.; Revol-Cavalier, F.; Thuair, A.; Agache, V. Separation of biological particles across 10X different length scales with cascaded deterministic lateral displacement modules, Sci Rep 8, 17762 (**2018**). <https://doi.org/10.1038/s41598-018-34958-8>

TOC GRAPHIC



for TOC only